Biomimetic flow control

# Stroke plane angle controls leading edge vortex in a bat-inspired flapper

Gide Koekkoek [a,b], Florian T. Muijres [a], L. Christoffer Johansson [a], Melanie Stuiver [a,b], Bas W. van Oudheusden [b], Anders Hedenström [a,*]

[a] *Lund University, Department of Biology, Ecology Building, SE-223 62 Lund, Sweden*
[b] *Delft University of Technology, Department of Aerospace Engineering, P.O. Box 5058, 2600 GB Delft, The Netherlands*

## A R T I C L E   I N F O

## A B S T R A C T

The present interest in micro air vehicles has given the research on bat flight a new impulse. With the use of high speed cameras and improved PIV techniques, the kinematics and aerodynamics of bats have been studied in great detail. A robotic flapper makes it possible to do measurements by systematically changing only one parameter at a time and investigate the parameter space outside the natural flight envelope of bats without risking animal safety. For this study, a robotic flapper (RoBat), inspired by *Leptonycteris yerbabuenae* was developed and tested over the speed range 1–7 m/s, with variable maximum angles of attacks ($AoA_{max} = 55°$ and $15°$, respectively) and constant $AoA_{max} = 55°$. These measurements show the presence of a leading edge vortex (LEV) for low speeds and a fully attached flow for high speeds at low $AoA_{max}$, which is in line with natural bat flight. A LEV occurs for $AoA_{max} = 55°$ throughout the complete flight speed range, and throughout which the LEV circulation coefficient remains rather constant. This implies that bats and micro air vehicles could use LEVs for high load maneuvers also at relatively high flight speeds. However, at high flight speeds the LEV bursts, which causes increased drag, most likely due to a decrease in Strouhal number.

© 2011 Académie des sciences. Published by Elsevier Masson SAS. All rights reserved.

## 1. Introduction

The present interest in flapping micro air vehicles (MAV) has resulted in a renewed interest in animal flight (e.g. Lentink and Biewener [1]). The maneuverability and hover capability of animals is still unrivaled by MAVs, suggesting that animal flight can still act as a source of inspiration for future MAV designs. Bats are of particular interest because of their impressive maneuverability and similarity to MAVs regarding size and often also airframe design, consisting of flexible wing membranes spanned between stiffeners (e.g. www.delfly.nl).

Recent studies of kinematics and aerodynamics of bat flight have considerable increased our understanding of bat flight (Hedenström et al. [2,3], von Busse [4], Tian et al. [5], Johansson et al. [6], Muijres et al. [7], Hubel et al. [8,9], Wolf et al. [10], Muijres et al. [11], Lindhe-Norberg and Winter [12], Muijres et al. [13]). With the use of high speed cameras the kinematics of bats flying in a wind tunnel are analyzed and show that the motion of the wings contain next to a flapping, also a yawing, contracting and pitching component (Wolf et al. [10], von Busse [4]). In addition, the camber, angle of attack (AoA) and orientation of the leading edge flap (LEF, part of the wing membrane controlled by the thumb and index finger, Propatagium and Dactylopatagium brevis) all show a substantial variation indicating an active control of the flow (von Busse [4]).

---

* Corresponding author.
  *E-mail address:* anders.hedenstrom@biol.lu.se (A. Hedenström).

The airflow structure close to the top surface of the wing of *G. soricina* bats has been measured using Particle Image Velocimetry (PIV) in imaging planes parallel to the flight direction (Muijres et al. [7]), which revealed the presence of an attached leading edge vortex (LEV) that produced about 40% of the lift during slow flight (1 m/s). The LEV is present at mid downstroke over the complete wing span, with the highest strength near the wingtip. The LEV is stably attached at least up to mid downstroke, although in steady conditions the high angle of attack (around 51 degrees) should cause full separation (Laitone [14]).

It is still largely unknown how bats control the attached LEV, such as the relation between the kinematics and LEV stability, and whether the control mechanism is due to passive deformation or active control of the wing shape. It has recently been shown that bats have sensory hairs on the top surface of the wing that are specialized in sensing reversed airflow (Chadha et al. [15], Sterbing-Dangelo et al. [16]). Thus, bats should have the ability to sense LEV separation, which indicates that LEV control in bats could potentially at least be partly active.

The difficulty with doing measurements with live animals is that a parametric study is very hard or even impossible to achieve and animal safety gives restrictions. For these reasons computational approaches are ways around these problems (e.g. Soueid et al. [17], Sudhakar and Vengadesan [18]). Another solution could be to use a robotic flapper that will not have these limitations and thereby could give new information about bat flight and provides the possibility to explore aerodynamic regions outside the natural flight envelope of bats. Robotic models inspired by a fruit fly (e.g. Dickinson et al. [19]) and a goose (Hubel and Tropea [20,21]) have already proven to be interesting study objects, while to the best of our knowledge so far no aerodynamic data have been published derived from a bat-inspired flapping model. One very promising bat-inspired model is the BATMAV (Bunget [22]), but no aerodynamic data have yet been published.

In this article a robotic bat-inspired flapper (RoBat) is used to mimic flight kinematics of *Leptonycteris yerbabuenae* (*L. yerbabuenae*) at 5 m/s flight speed as closely as possible. The aim was to determine how the LEV can be controlled using simple adjustments in the stroke plane angle and give information concerning the AoA and Strouhal number dependencies of separation and LEV in bat-inspired wings. We use two test cases, one where the stroke plane angle is changed with flight speed resulting in similar AoAs as measured in real bat flight, and a second case where the AoA at mid downstroke ($AoA_{max}$) is kept constant. Both cases were studied across a flight speed range of 1 to 7 m/s. In order to evaluate the utility of a mechanical flapper we focused on one important aerodynamic feature of bat flight, i.e. the LEV (Muijres et al. [7]). A more complete study of the aerodynamics of this bat flapper is left for a future project.

## 2. RoBat wing design

The RoBat design is based on the geometry and kinematics of the *L. yerbabuenae* bat (von Busse [4]). *L. yerbabuenae* is a medium sized (20–25 g) tropical nectar feeding bat. It is well adapted to hovering flight, which it does when feeding from flowers. Since *L. yerbabuenae* is a migratory species and travels up to 100 km every night from roost to feeding patches, it can be assumed well adapted to efficient cruising flight (Horner et al. [23]). Thus, *L. yerbabuenae* can operate efficiently throughout a wide velocity range from hovering (0 m/s flight) up to a flight speed of at least 8 m/s (Sahley et al. [24], Horner et al. [23]).

Along this velocity range, the wingbeat frequency of *L. yerbabuenae* ranges from about 13 Hz (hovering) to about 9 Hz (fast forward flight). To be able to reach these kinds of frequencies with a mechanical flapper, powerful and very precise actuators are required. Also vibrations, especially around the eigenfrequencies can be expected to cause problems. To reduce the flapping frequency of the mechanical flapper, the model was designed as an isometric scale of 1:2 of an *L. yerbabuenae* wing. Using this scaling will decrease the frequency with a factor of 4 (see below). Two other advantages of scaling up the model are that a larger model is easier to produce and that more measurements per wingbeat will increase the time resolution. When scaling a wing geometrically, also the aerodynamic and mechanical parameters need to be scaled appropriately.

### 2.1. Scaling of the RoBat wing

For aerodynamic similarity between the bat wing and the scaled model both the Reynolds number (*Re*) and Strouhal number (*St*) should be kept constant. *Re* is a measure of the relative inertial and viscous forces produced by a wing with characteristic length scale *l*, defined as

$$Re = \frac{U_{\infty,eff}l}{\upsilon} \tag{1}$$

where $U_{\infty,eff}$ is the effective velocity at which the wing operates (Fig. 1), defined by

$$U_{\infty,eff} = \sqrt{(U_\infty + U_{flap,x})^2 + U_{flap,z}^2} \tag{2}$$

$\upsilon$ is the kinematic viscosity of air, $U_{flap,x}$ the horizontal and $U_{flap,z}$ the vertical component of $U_{flap}$, i.e. the wing flapping velocity in the wind tunnel frame of reference. See Fig. 4 for the definition of the coordinate system. If *Re* is kept constant during scaling, then
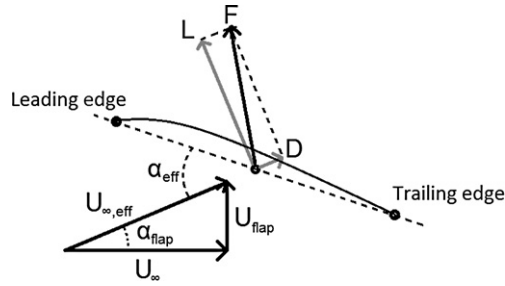
$$U_{\infty,eff} \propto l^{-1} \tag{3}$$

**Fig. 1.** Cross section of the flapping RoBat wing. Definition of forces: aerodynamic force $F$, with lift $L$ and drag $D$ components. Definition of velocities: free stream velocity $U_\infty$, effective velocity $U_{\infty,eff}$ and flap velocity $U_{flap}$. Definition of angles: inflow angle ($\alpha_{flap}$) and angle of attack ($\alpha$).
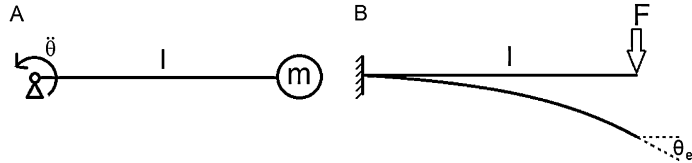


**Fig. 2.** (A) point mass with mass $m$ at distance $l$ from the rotation point with angular acceleration ($\ddot{\theta}$). (B) Clamped beam with force $F$ on length $l$ and elastic deflection angle $\theta_{el}$.

Since, for similarity the angle of incidence, $\alpha_{flap}$, should be kept constant (Fig. 1), the free stream velocity $U_\infty$ scales linearly with $U_{\infty,eff}$. Thus,

$$U_\infty = \cos(\alpha_{flap}) \cdot U_{\infty,eff} \quad \Rightarrow \quad U_\infty \propto l^{-1} \tag{4}$$

For our model this means $U_{\infty,model} = U_{\infty,bat}/2$. From now on, when referring to velocities we will use the equivalent air speed

$$U_{eq} = U_{bat} = 2U_{model} \tag{5}$$

Keeping $Re$ constant has the consequence that the forces are not affected by the scaling of the model

$$L = \frac{1}{2}C_L \rho_{air} S U_{\infty,eff}^2 \propto l^2 (l^{-1})^2 = \text{constant} \tag{6}$$

where $C_L$ is the lift coefficient, $\rho_{air}$ is the density of air and $S$ is the surface of the wing.

$St$ is a measure of the relative importance of unsteady aerodynamic effects for flapping wings, and defined here as

$$St = \frac{fl}{U_{\infty,eff}} \tag{7}$$

where $f$ is the flapping frequency. To keep $St$ constant during scaling, $f$ should scale with $l^{-2}$

$$f \propto \frac{U_{\infty,eff}}{l} \propto l^{-2} \tag{8}$$

Thus, for our model $f_{model} = f_{bat}/4$. To be able to model wing deformations correctly, the ratio between fluid dynamic forces and mechanical forces of the wing (inertia and elastic forces) should be kept constant. $L$ is unaffected by the scaling (Eq. (6)), thus the mechanical forces should be kept constant too. Assuming, for scaling purposes, a simplified mechanical model, with a concentrated mass $m$ representing the wing and a total force $F$, both located at a distance $l$ from the hinge ('shoulder') point (Fig. 2). The mechanical forces can be modeled as

$$F_{elastic} \propto \theta_{el} = \frac{Fl^2}{2EI} = \text{constant}, \quad \text{and} \tag{9}$$

$$F_{inertia} = ma = m\ddot{\theta}l \propto \rho_{wing}d^2 l\ddot{\theta}l = \text{constant} \tag{10}$$

where $F_{elastic}$ is the elastic force, $F_{inertia}$ is the inertial force, $\ddot{\theta}$ is the angular acceleration, $\rho_{wing}$ is the density of the wing skeletal bones, $d$ is the diameter of the wing bones, $\theta_{el}$ is the elastic deformation angle, $E$ is Young's modulus and $I$ is the area moment of inertia. Note that, for simplicity, the mass of the membrane is neglected.

When scaling a periodic flapping motion with the angular amplitude kept constant, the angular acceleration scales with $f^2$, which gives

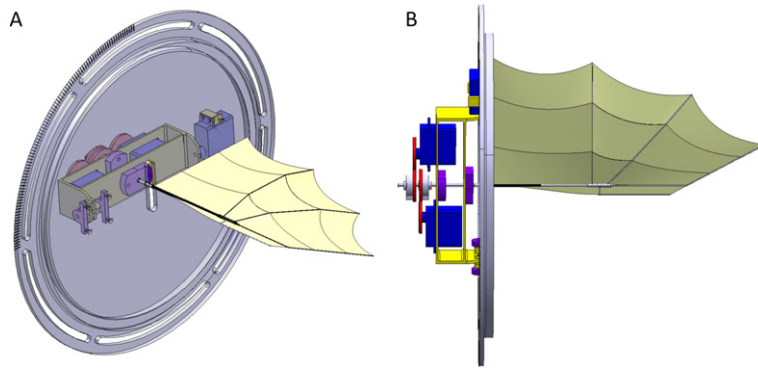$$\ddot{\theta} \propto f^2 \propto l^{-4} \tag{11}$$

**Fig. 3.** The RoBat wing, drive system and mounting plate. The drive system components are cogwheels (red), servos (blue), support structure (yellow), bearings (purple) and axes (grey). (For interpretation of the references to color in this figure legend, the reader is referred to the web version of this article.)

By substituting Eq. (11) into Eq. (10) the scaling of $\rho_{wing}d^2$ can be determined as

$$\rho_{wing}d^2 \propto \frac{1}{l\ddot{\theta}l} \propto \frac{1}{ll^{-4}l} \propto l^2 \tag{12}$$

Using a circular cross section gives the scaling of the second moment of inertia as

$$I = \frac{\pi d^4}{64} \propto d^4 \tag{13}$$

Combined with Eq. (9) this gives the scaling for $Ed^4$ as

$$Ed^4 \propto Fl^2 \propto l^2 \tag{14}$$

Both Eqs. (12) and (14) must now be used to select the material and dimensions of the model wing. They can only be fulfilled when the density, Young's modulus or both are changed with respect to the values for a real bat. In practice $\rho_{wing}$ and $E$ cannot be changed independently due to the limited range of available materials. Therefore, we made a trade-off between $\rho_{wing}$, $E$, and $d$ for our model wing as discussed below.

### 2.2. The RoBat wing geometry and materials

A bat wing consists of compliant skin membranes spanned between stiffeners consisting of elongated hand digits (Swartz et al. [25]). The membrane is anisotropic and varies in thickness and stiffness over the wing. There are also muscles running through the membrane that make active control of the membrane stiffness possible (Swartz et al. [26]).

The bat wing membranes are modeled by a 0.25 mm thick latex sheet, and the stiffeners are constructed using carbon reinforced epoxy (63% fiber volume) rods. These rods give an average value of $Ed^4$ that is a factor 30 higher than the average value in bats and $\rho d^2$ that is 10% lower than in bats (Table 2, Swartz and Middleton [27]). This means that the wing is designed relatively stiff with respect to the real bat, while the mass of the RoBat bones is comparable with that of real bats. The difference in stiffness is a result of the limited choice in useful building materials. Since bone stiffness varies much throughout a bat wing (Swartz and Middleton [27]) an exact match in stiffness is almost impossible, and therefore we assumed it was safer to design the RoBat wing too stiff rather than too compliant.

The dimensions of the model wing were based on the wing geometry *L. yerbabuenae* at mid downstroke, estimated from kinematics measurements of *L. yerbabuenae* flying at 5 m/s in a wind tunnel (von Busse [4]). The first and second bat wing digits were combined into the LEF (Fig. 3).

### 2.3. The RoBat wing kinematics

Based on the wing kinematics of *L. yerbabuenae* (von Busse [4]), we decided to model three motions; a wing flapping motion, a wing pitching motion, and an LEF deflection motion. The flapping motion is the main motion for inducing $U_{flap}$. It is supplemented by the pitching motion to be able to regulate the AoA. The LEF rotation is added, since it is regarded as important for the control of profile shape in bat wings (von Busse [4]).

For each motion, a dedicated servo motor (Hitec HS-7940TH, 7.2 V) was used. The flapping motion is transferred from servo to wing through a direct connection, while for both the pitching motion and LEF deflection a cogwheel system was used (Fig. 3). The whole structure was connected to a circular aluminum plate placed in the wind tunnel sidewall, which can be rotated manually to adjust the stroke plane angle of the model (Fig. 3).

**Table 1**
Kinematic parameters used for the experimental measurements.

| $U_{eq}$ [m/s] | Required $AoA_{max}$ [degree] | Stroke plane angle [degree] | Reynolds number $Re_{tip}$ [–] | Strouhal number $St_{tip}$ [–] |
|---|---|---|---|---|
| 7 | 15 | 12 | 2.5E4 | 0.19 |
| 5 | 20 | 17 | 1.9E4 | 0.25 |
| 3 | 35 | 27 | 1.4E4 | 0.35 |
| 2 | 45 | 42 | 1.2E4 | 0.42 |
| 1 | 55 | 52 | 8.8E3 | 0.55 |
| 2 | 55 | 65 | 1.2E4 | 0.39 |
| 3 | 55 | 70 | 1.6E4 | 0.31 |
| 5 | 55 | 73 | 2.2E4 | 0.22 |
| 7 | 55 | 74 | 2.9E4 | 0.17 |

**Table 2**
Morphological data of *Leptonycteris yerbabuenae* and of the RoBat.

| Measure | Unit | *L. yerbabuenae* | RoBat |
|---|---|---|---|
| Semispan | [m] | 0.16 | 0.29 |
| Wing area | [m$^2$] | 0.016 | 0.058 |
| Mean chord | [m] | 0.047 | 0.10 |
| Aspect ratio | [–] | 7.0 | 5.6 |
| Density bones | [kg/m$^3$] | 2000[*] | 1590 |
| Young's modulus bones | [GPa] | 20–23[**] | 140 |
| Radius bones | [mm] | 1.4[**] | 3 |
| Young's modulus membrane | [MPa] | 3–37[***] | 1.5 |
| Thickness membrane | [mm] | 0.22–0.28[***] | 0.25 |

[*] Dumont [33];
[**] Swartz and Middleton [27];
[***] Swartz et al. [26].

The three motions described previously are optimized based on the kinematics data from *L. yerbabuenae* flying at 5 m/s (von Busse [4]). The kinematics of the LEF could be directly fitted with a sinusoidal motion (Fig. S1, see section Supplementary material), but because the flapping and pitching motions in real bat flight are not generated by two purely rotational motions, but instead by multiple hinges as well as wing deformations (Swartz et al. [25]), the flapping and pitching motions were optimized using the optimization scheme presented in Fig. S2.

Two aerodynamic parameters were used in the optimization, being AoA and inflow angle $\alpha_{flap}$ (Fig. 1). These variables were chosen because AoA primarily characterizes the aerodynamic structure and force production generated by a wing and inflow angle primarily characterizes the direction of the force vector *F*.

The computer model calculated the aerodynamic parameters (AoA and $\alpha_{flap}$) using the given motions and geometry of the wing. Using the desired AoA (AoA$_{ref}$) as parameter for the pitching motion and $\alpha_{flap,ref}$ for the flapping motion the wing kinematics was thereby optimized. The resulting flapping and pitching motions for the model were then fitted with the sum of three sinusoidal motions, which could be generated by the servo motors (Fig. S3).

### 2.4. The measurement sequences

To be able to investigate the influence of AoA and *St* on the performance of flapping bat wings, two sets of measurements were done, both with the above described wing kinematics based on *L. yerbabuenae* at 5 m/s. Both sets of measurements were done throughout an equivalent flight speed range from 1 m/s to 7 m/s (increments of 1 m/s), see Table 1. In the first case the stroke plane of the flapper was adjusted so the maximum AoA within the wingbeat (AoA$_{max}$) was equal to that of *L. yerbabuenae* throughout the flight speed range (AoA$_{max}$ = 55° at 1 m/s to AoA$_{max}$ = 15° at 7 m/s), hereafter called the variable AoA$_{max}$ case. In the second set of experiments the AoA$_{max}$ was kept constant throughout the flight speed range (AoA$_{max}$ = 55°, based on *L. yerbabuenae* at 1 m/s), hereafter called the constant AoA$_{max}$ case. The stroke plane angles required to obtain the desired AoA$_{max}$ were calculated using simplified trigonometry. Note that changing the stroke plane angle to optimize AoA$_{max}$ will also change the pitching angle relative to the wind tunnel frame of reference.

The Reynolds number in Table 1 is calculated using Eqs. (1) and (2) based on the mean chord and mean flap velocity of the wing tip over the downstroke. The Strouhal number in Table 1 is calculated using Eqs. (2) and (7) based on the wing tip and the mean flap velocity of the wing tip over the downstroke.

## 3. Test set-up

For this study measurements were made in the Lund University closed loop, low turbulence and low speed, wind tunnel (Pennycuick et al. [28]). The model was attached to the wall of the wind tunnel test section that influences the velocity up to 3 cm and the turbulence of the airflow up to 10 cm from the wall at 10 m/s (Pennycuick et al. [28]), which is 10%
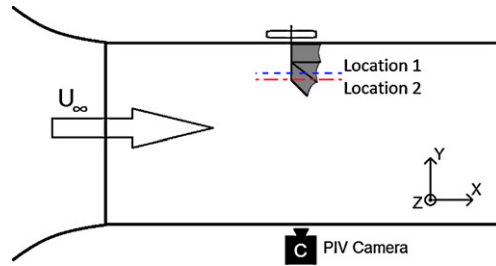
**Fig. 4.** Top view of the test section of the wind tunnel with the RoBat model, PIV camera, the free stream velocity vector ($U_\infty$) and definition of the wind tunnel coordinate system.
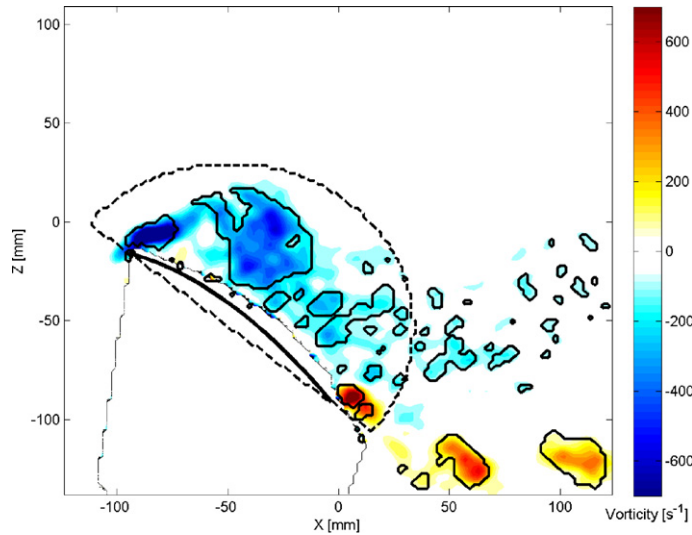


**Fig. 5.** Vorticity field around the flapping RoBat wing (AoA = 48° and $U_{eq} = 5.2$ m/s) with swirl strength contours (solid line) and semicircle domain (dashed line), within which the circulation is measured.

and 34% of the semi-span, respectively. The PIV system consisted of a 200 Hz 50 mJ Laser (Litron LPY732 series, Nd:YAG, 532 mm) for illumination of fog particles (1 μm diameter), a CMOS-camera (High-SpeedStar3; 1024 × 1024 pixels) and a frame grabber PCI board in a host computer. The laser sheet was aligned with the flow in the $xz$-direction and the camera was positioned outside the test section at the opposite side of the model to be able to capture the flow field above the wing with minimum shadows and reflections (Fig. 4). Measurements were performed at two spanwise wing locations, called the inner wing position (at 51% semi-span) and the outer wing position (63% semi-span).

## 4. Data analysis

Both aerodynamic and kinematic data were gathered from the images recorded by the PIV camera. The kinematics of the leading and trailing edges of the wing at the measured cross section were manually tracked with software described in Hedrick [29]. From these two points the pitching angle and the velocity of the midpoint were determined, which is used to determine the AoA, local Reynolds, Strouhal and Rossby number. The aerodynamic data were gathered from analyzing the PIV images using DaVis (7.4.0.122) with a multi-pass 2D cross-correlation (32 × 32, 16 × 16, 50% overlap) and a 3 × 3 smoothing average post-processing. From every period one frame was selected and analyzed resulting in nine frames per measurement with close to identical geometry and phase because of the repetitive motion of the model. These nine frames were averaged using Davis and analyzed with a custom made Matlab (7.11.0.584, R2010b) routine to determine the circulation. For every set-up 5 measurements were done that were used to calculate a mean value and a standard deviation (Fig. S4). The circulation was determined above the wing cross section using a semicircle determined by the line through the two points obtained from the kinematics and 70% of the local chord as radius to be able to capture all the relevant vortices (Fig. 5). Because of the turbulent character of the flow fields at high angles of attack (Fig. 5) we chose to use the swirling strength ($\lambda_{el}$) criterion for identifying vortices (Adrian et al. [30]). The swirling strength is determined by the imaginary part of the eigenvalues of the two-dimensional gradient tensor. The gradient tensor is determined by

$$D = \begin{pmatrix} \frac{\partial u_1}{\partial x_1} & \frac{\partial u_1}{\partial x_2} \\ \frac{\partial u_2}{\partial x_1} & \frac{\partial u_2}{\partial x_2} \end{pmatrix} \tag{15}$$
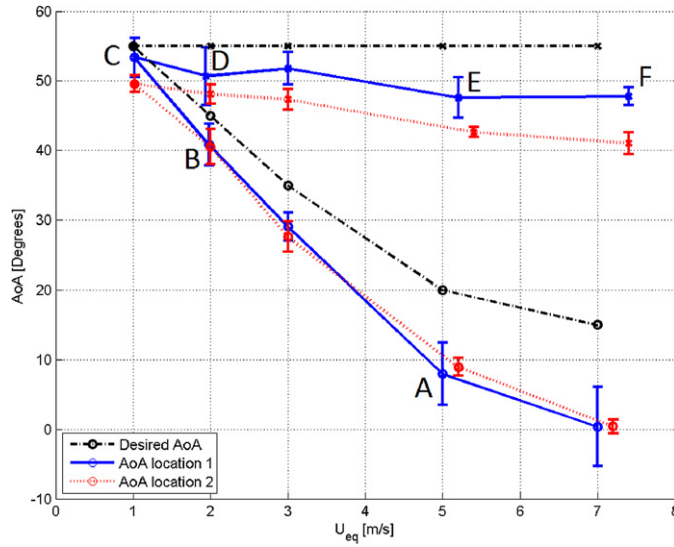
**Fig. 6.** Angle of attack versus equivalent free stream velocity $U_{eq}$ (means $\pm$ standard deviation). The labels A–F refer to the panels in Fig. 7.

In this case negative vorticity was used for the circulation ($\Gamma$) if the swirling strength was larger than 5% of the maximum (Fig. 5) and the total area within these boundaries is used as a measure for the size of the vortices ($S_\omega$). The circulation was used to calculate the circulation coefficient

$$C_\Gamma = \frac{\Gamma}{U_{\infty,eff} \cdot c_{loc}} \tag{16}$$

Based on the measured wing kinematics the local Reynolds number $Re_{loc}$, local Strouhal number $St_{loc}$ and the local Rossby number $Ro_{loc}$ (Lentink [31]) were calculated from Eqs. (17)–(19).

$$Re_{loc} = \frac{c_{loc} U_{\infty,eff}}{\upsilon} \tag{17}$$

where $c_{loc}$ is the local chord length.

$$St_{loc} = \frac{0.5 U_{wing,z}}{U_\infty + U_{wing,x}} \tag{18}$$

with $U_{wing,z}$ being the local $z$ component of the wing velocity and $U_{wing,x}$ the local $x$ component of the wing velocity. The Rossby number is defined as

$$Ro_{loc} = \frac{U_{\infty,eff}}{\dot{\theta}_{loc} c_{loc}} = \frac{U_{\infty,eff} \cdot R_{loc}}{U_{wing} \cdot c_{loc}} \tag{19}$$

where $\dot{\theta}_{loc}$ is the local angular velocity, $R_{loc}$ is the local semi-span. The Rossby number is a measure for the importance of the Coriolis acceleration due to rotation in the flapping motion.

## 5. Results

The resulting $AoA_{max}$ for the two spanwise wing positions are shown in Fig. 6 together with the desired $AoA_{ref}$ based on the kinematics of *L. yerbabuenae*, throughout the measured flight speed range. It is clear that $AoA_{max}$ is generally lower than the desired value, and this error increases both along the wingspan and with $U_{eq}$.

### 5.1. Description of the flow field

The vorticity values and instantaneous streamlines in the wing fixed reference frame for different flow fields are shown in Fig. 7. The flow field in a wing fixed reference frame gives primarily information about the aerodynamic state of the flow, and especially flow separation from the wing. The wing fixed reference frame flow fields were determined by subtracting the wing velocity in the $xz$-plane from the flow fields in the wind tunnel fixed reference frame.

Starting at $AoA_{max} = 8°$ and $U_{eq} = 5$ m/s a quasi steady state is visible with very low values of vorticity (Fig. 7A). The slightly curved streamlines indicate some lift production, which corresponds with the low $AoA_{max}$. At $AoA_{max} = 41°$ and $U_{eq} = 2.0$ m/s (Fig. 7B) a clear separation bubble at the leading edge is visible with flow reattachment halfway along
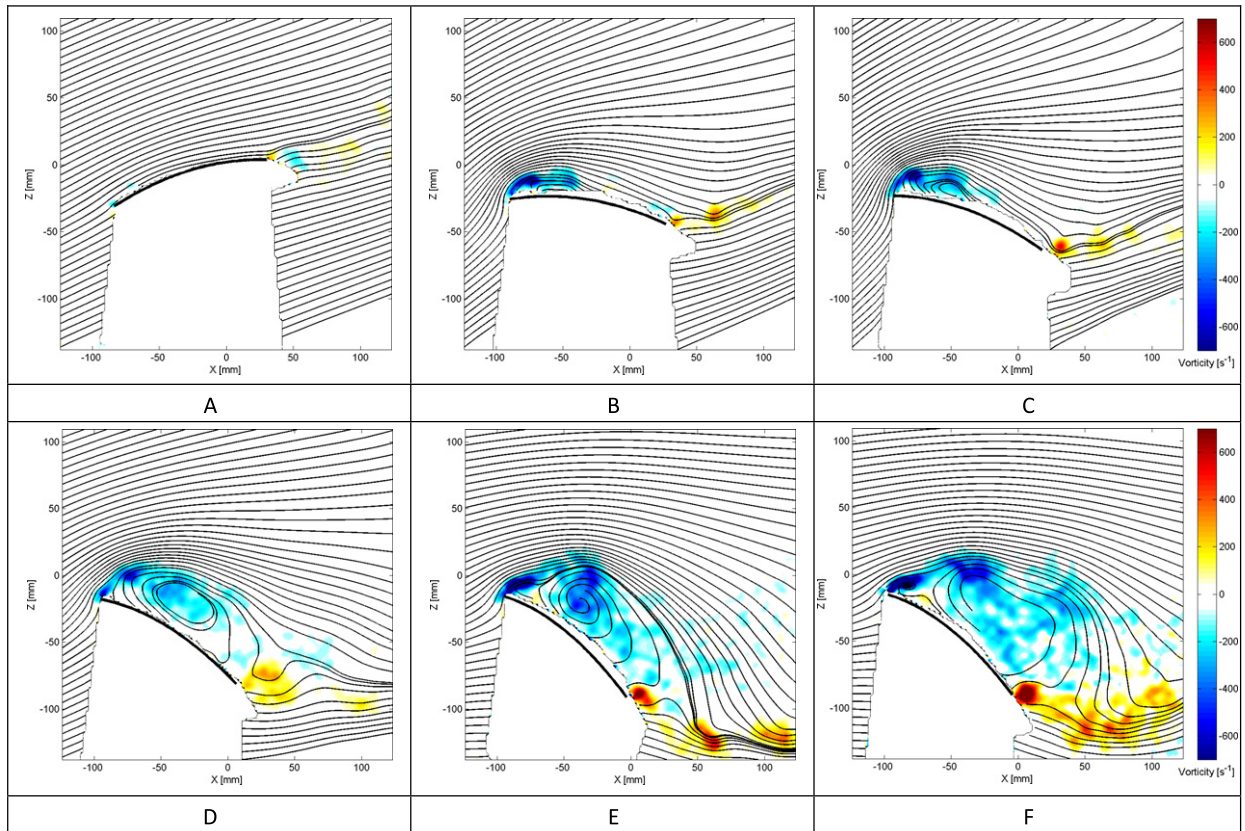
**Fig. 7.** Instantaneous streamlines and vorticity at the inner wing position. The values for the different panels are (A) AoA = 8°, $U_{eq}$ = 5.0 m/s; (B) AoA = 41°, $U_{eq}$ = 2.0 m/s; (C) AoA = 53°, $U_{eq}$ = 1.0 m/s; (D) AoA = 51°, $U_{eq}$ = 2.0 m/s; (E) AoA = 48°, $U_{eq}$ = 3.1 m/s; (F) AoA = 48°, $U_{eq}$ = 7.4 m/s.

the chord. The trailing edge vortices, of opposite sense to the LEF, that are shed indicate an increase in lift production by the wing throughout the downstroke. At $AoA_{max}$ = 53° and $U_{eq}$ = 1.0 m/s (Fig. 7C) the LEV has increased in size but reattachment still occurs upstream of the trailing edge. At $AoA_{max}$ = 51° and $U_{eq}$ = 2.0 m/s (Fig. 7D) the vorticity above the wing has suddenly greatly increased, reattachment does not occur anymore, and the vortices that are generated at the leading edge of the wing are periodically shed into the wake. These characteristics are indicative of LEV bursting (Lentink and Dickinson [32]). The burst vortex wake increases in size consistently with increasing flight speed (Fig. 7E: $AoA_{max}$ = 48°, $U_\infty$ = 2.6 m/s, and Fig. 7F: $AoA_{max}$ = 48°, $U_\infty$ = 3.7 m/s). Note that vortex bursting is a result of the change in $U_{eq}$, since the $AoA_{max}$ stays nearly constant in the cases shown in Fig. 7C–F.

### 5.2. Vortex dynamics

The circulation coefficients ($c_\Gamma$) determined from the vortices positioned above the wing are plotted against $Re_{loc}$, $AoA_{loc}$ and $St_{loc}$ and $Ro_{loc}$ in Fig. 8A–D, respectively, as well as for the vorticity area ($S_\omega$) in Fig. 9A–D, respectively.

The increase in $c_\Gamma$ occurs at an almost constant $Re_{loc}$ (variable $AoA_{max}$ measurements in Fig. 8A), while $c_\Gamma$ remains constant with increasing $Re_{loc}$ (constant $AoA_{max}$ measurements in Fig. 8A). This shows that $c_\Gamma$ is largely independent from $Re_{loc}$. The same is almost valid for $S_\omega$ although $S_\omega$ remains increasing for the constant $AoA_{max}$ measurements with increasing $Re_{loc}$ (Fig. 9A).

Fig. 8B shows that $c_\Gamma$ is associated with $AoA_{max}$. For the variable $AoA_{max}$ measurements, a weak LEV starts to occur at $AoA_{max}$ = 30°, and its strength ($c_\Gamma$) and size ($S_\omega$) increases almost linearly with $AoA_{max}$ up to $AoA_{max}$ > 50° (Fig. 8B). For the constant $AoA_{max}$ measurements, $c_\Gamma$ initially increases with flight speed (Fig. 8B, label C–D), but then remains rather constant with further increased speed (Fig. 8B, label D–F). The vortex size ($S_\omega$) increases by a factor 3–4 for the constant $AoA_{max}$ measurements.

The largest increase in $c_\Gamma$ occurs also at a constant $St_{loc}$ (∼ 0.3, variable $AoA_{max}$ measurements in Fig. 8C), while $c_\Gamma$ remains almost constant when $St_{loc}$ decreases from 0.2 to 0.05 (constant $AoA_{max}$ measurements in Fig. 8C). Thus, $c_\Gamma$ is also largely independent from $St_{loc}$. In contrast, $S_\omega$ seems to be $St_{loc}$ dependent because for data points where $S_\omega$ is increasing the most $St_{loc}$ is decreasing almost linearly (Fig. 9C).

The shape of the $c_\Gamma$–$Ro_{loc}$ and $S_\omega$–$Ro_{loc}$ curves (Fig. 8D and 9D) are comparable with the $c_\Gamma$–$Re_{loc}$ and $S_\omega$–$Re_{loc}$ curves.
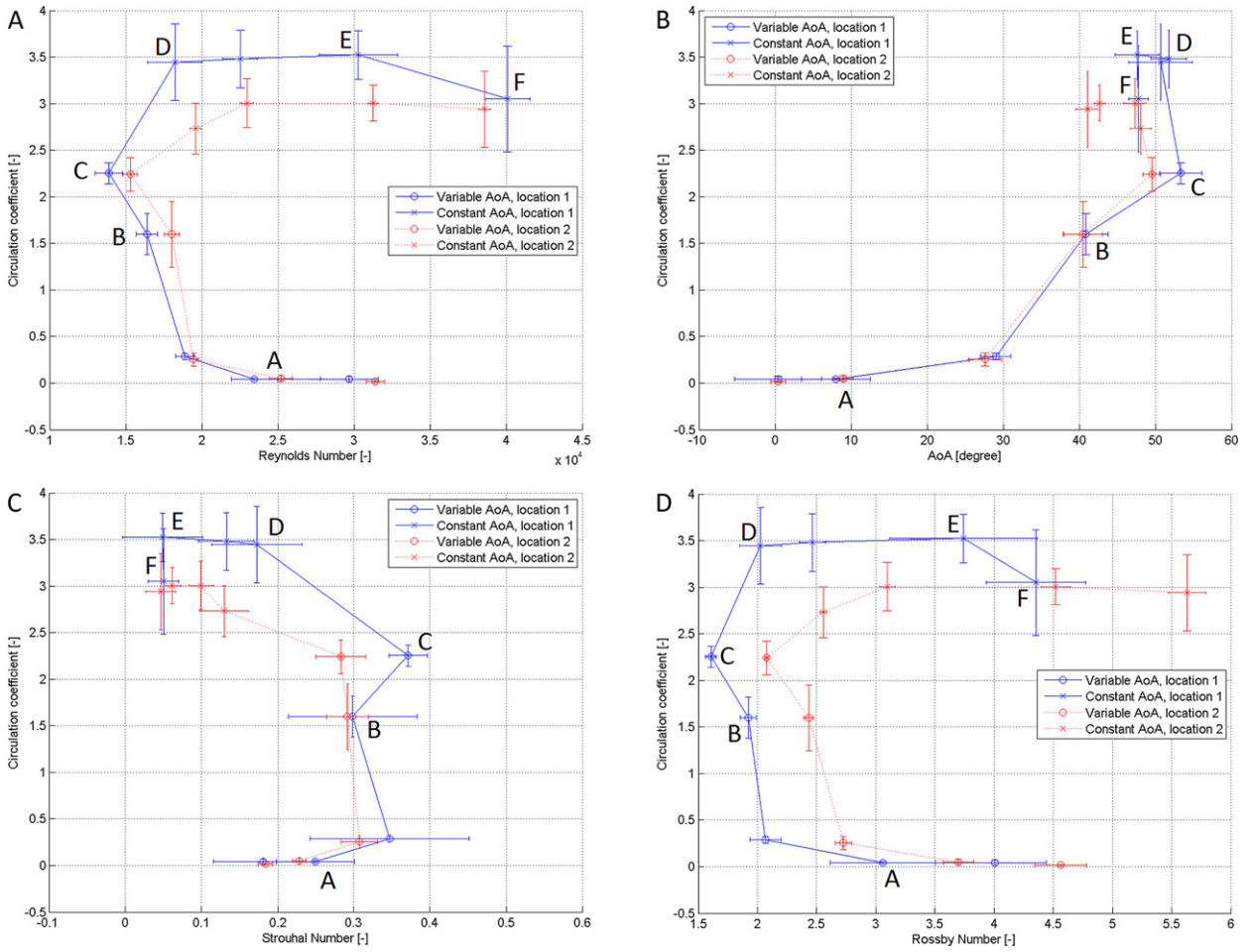
**Fig. 8.** Circulation coefficient (means ± standard deviation) of vortex structure above the wing with respect to $Re_{loc}$ (A), $AoA_{max}$ (B), $St_{loc}$ (C) and $Ro_{loc}$ (D). The labels A–F refer to the panels in Fig. 7.

## 6. Discussion

### 6.1. RoBat model

Although the RoBat model does not capture the full complexity of either real bat wing kinematics or wing morphology, we show that the simplified kinematics of the RoBat, based on sinusoidal flapping, pitching and leading edge flap deflection, can be used as model to study fluid dynamics mechanisms relevant for bats.

Across the complete studied flight speed range, the resulting $AoA_{max}$ was lower in the model than that of real bats. This discrepancy was largest at high $U_{eq}$ and at the spanwise, more distal, wing position. Therefore, we can assume that the reduction in $AoA_{max}$ for the RoBat is due to spanwise pitch down wing twist as a result of lift production. These aeroelastic effects were not captured by our kinematics optimization scheme, resulting in the overestimation of the $AoA_{max}$ in the RoBat.

### 6.2. Vortex dynamics

The test sequence with variable $AoA_{max}$ represents a steady flight of bats and shows no LEVs at high speeds and a strong stable attached LEV at low speeds. This transition is primarily due to an increase in $AoA_{max}$ with decreasing flight speed, which parallel the conditions when real bats exhibit a LEV (Muijres et al. [7]).

The constant $AoA_{max}$ sequence showed that, throughout the complete flight speed range, it is possible to generate a LEV by operating at a high enough $AoA_{max}$, and that the strength of the LEV structure ($c_{\Gamma}$) stays nearly constant at constant $AoA_{max}$ throughout the complete measured flight speed range. The structure and size of the LEV vary significantly with flight speed, which can be explained by a change in $St_{loc}$, and independent from $Re_{loc}$.
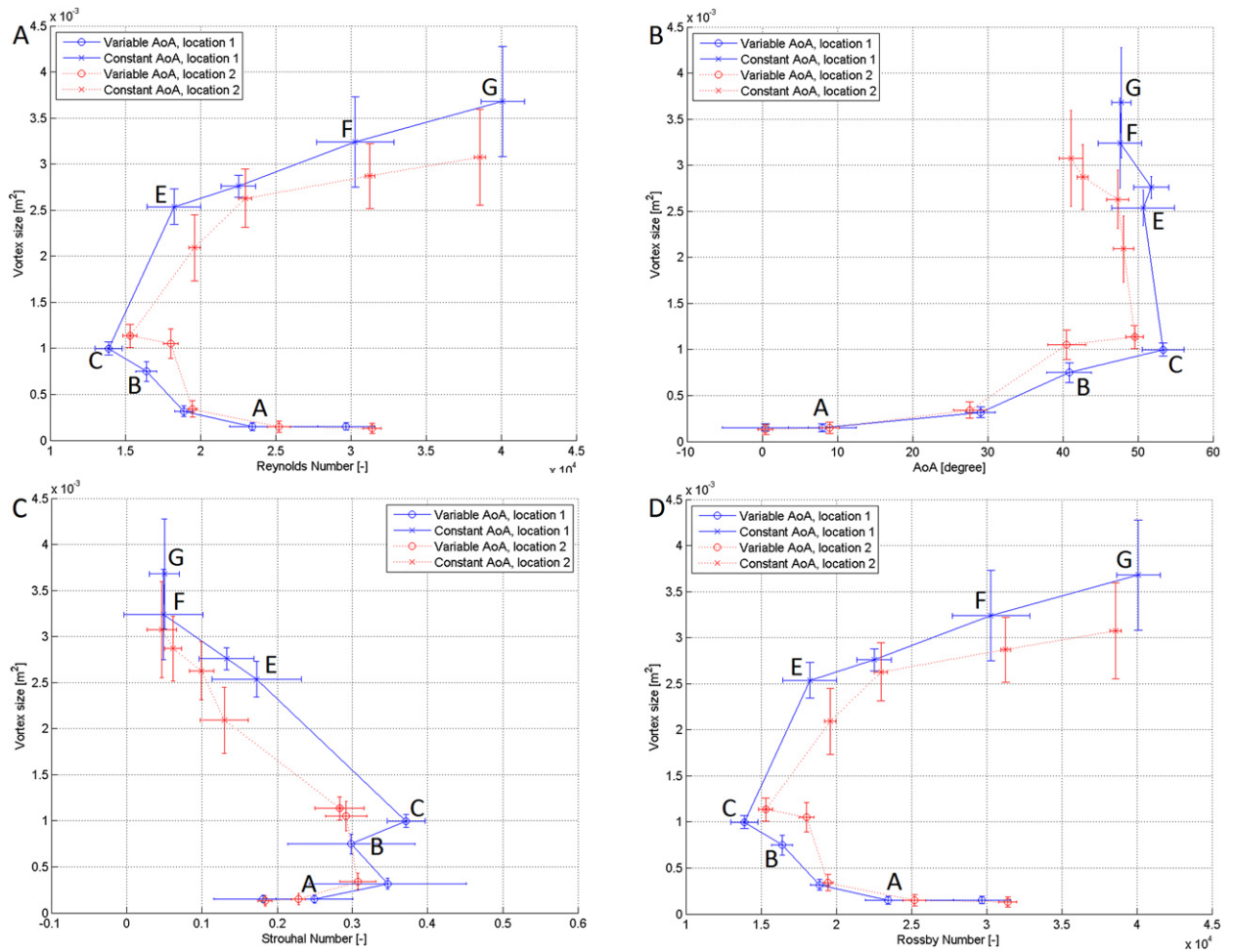
**Fig. 9.** Cumulative area (means ± standard deviation) of the vortex structures above the wing with respect to $Re_{loc}$ (A), AoA$_{max}$ (B), $St_{loc}$ (C) and $Ro_{loc}$ (D). The labels A–F refer to the panels in Fig. 7.

### 6.3. Relevance for bats

Based on lift coefficient estimates for flying *L. yerbabuenae* (Muijres et al. [11]) an enhanced lift mechanism, such as a LEV, can be expected at low flight speeds ($C_{L\max} > 1.6$ for $U_{eq} < 4$ m/s), but not at high flight speeds ($C_{L\max} < 1.6$ for $U_{eq} > 4$ m/s) (Laitone [14]). This corresponds well with the results obtained in the present study. Also, the LEV structure found at $U_{eq} = 1$ m/s was similar to that found in a smaller species of bat *G. soricina* (Muijres et al. [7]).

LEVs can enhance $C_L$, but this comes with a penalty of increased drag (Lentink and Dickinson [32]). Therefore, we can assume that bats use LEVs at low flight speeds to generate enough lift for weight support. At cruising flight speeds the LEV is not required, and bats use the energetically more efficient attached flow at low AoA.

Still, bats are expected to be able to generate LEVs at high flight speeds by increasing AoA as shown by the present study, but it comes at a price, though, since the LEV tends to burst at high speeds, resulting in completely separated flow and high drag. Thus, LEVs could potentially be used by bats throughout the complete natural flight speed range in high load maneuvers such as sharp turns.

The increased sensitivity of the trailing edge part of the wing membrane for detecting reversed airflow as described recently (Chadha et al. [15], Sterbing-D'Angelo et al. [16]) could be used to sense LEV bursting. This information could be used by the bat to actively adjust wing kinematics to control the flow above the wing, which could possibly prevent LEV bursting and improve flight performance.

### 6.4. Relevance for MAVs

For the design of MAVs the fact that a single parameter, such as the stroke plane angle has such profound influence on the flow field and possibly the resulting flight forces is very interesting, especially since the stroke plane angle in an MAV can directly be controlled by changing its body angle.

The almost constant circulation coefficient around 50 degrees $AoA_{max}$ indicates that there is little influence of LEV bursting on the lift production, which makes it possible to use high AoA both at low and high speeds. However, lift enhancement by using LEVs will be less efficient at high speeds due to the expected increased drag from a bursted LEV.

### 6.5. Concluding remarks

Despite the complexity of the wing kinematics in bats we have been able to show that both bats and MAVs can extend their flight performance envelope by controlling only their body angle/stroke plane. This is accomplished by controlling the LEV lift production through changes of the AoA caused by the altered stroke plane. Further studies, incorporating higher complexity of the wing motion, will determine if this can be accomplished with higher efficiency by for example active control of the leading edge flap and camber of the wing.

We have shown that a mechanical bat model can be used to generate bat-like aerodynamic features, which in turn can be used to investigate the level of adaptation of morphology and kinematics as seen in real bats. To implement a bat-like MAV, possessing flight performance and control comparable to real bats, may require not only materials and kinematics properties similar to those in real bats, but also the implementation of wing-surface airflow sensors and the appropriate feedback to the actuating mechanism.

### Acknowledgements

### Supplementary material

The online version of this article contains additional supplementary material.
Please visit doi:10.1016/j.crme.2011.11.013.

### References

[1] D. Lentink, A.A. Biewener, Nature-inspired flight—beyond the leap, Bioinspiration & Biomimetics (2010) 040201, 9 pp.
[2] A. Hedenström, L.C. Johansson, M. Wolf, R. von Busse, Y. Winter, G.R. Spedding, Bat flight generates complex aerodynamic tracks, Science 316 (2007) 894–897.
[3] A. Hedenström, F. Muijres, R. von Busse, L.C. Johansson, Y. Winter, G.R. Spedding, High-speed stereo DPIV measurements of bat wakes flying freely in a wind tunnel, Experiments in Fluids 46 (2009) 923–932.
[4] R. von Busse, The Trinity of Energy Conversion: Kinematics, Aerodynamics and Energetics of Lesser Long-Nosed Bat (*Leptonycteris Yerbabuenae*), Humboldt University, Berlin, 2010.
[5] X. Tian, J. Iriarte-Diaz, K. Middleton, R. Galvao, E. Israeli, A. Roemer, A. Sullivan, A. Song, S. Swartz, K. Breuer, Direct measurements of the kinematics and dynamics of bat flight, Bioinspiration & Biomimetics 1 (2006) S10–18.
[6] L.C. Johansson, M. Wolf, R. von Busse, Y. Winter, G.R. Spedding, A. Hedenström, The near and far wake of Pallas' long tongued bat (Glossophaga soricina), Journal of Experimental Biology 211 (2008) 2909–2918.
[7] F.T. Muijres, L.C. Johansson, R. Barfield, M. Wolf, G.R. Spedding, A. Hedenström, Leading edge vortex improves lift in slow-flying bats, Science 319 (2008) 1250–1253.
[8] T.Y. Hubel, N.I. Hristov, S.M. Swartz, K.S. Breuer, Time-resolved wake structure and kinematics of bat flight, Experiments in Fluids 46 (2009) 933–943.
[9] T.Y. Hubel, D.K. Riskin, S.M. Swartz, K.S. Breuer, Wake structure and wing kinematics: The flight of the lesser dog-faced fruit bat, Cynopterus brachyotis, Journal of Experimental Biology 213 (2010) 3427–3440.
[10] M. Wolf, L.C. Johansson, R. von Busse, Y. Winter, A. Hedenström, Kinematics of flight and the relationship to the vortex wake of Pallas' long-tongued bat (Glossophaga soricina), Journal of Experimental Biology 213 (2010) 2142–2153.
[11] F.T. Muijres, L.C. Johansson, Y. Winter, A. Hedenström, Comparative aerodynamic performance of flapping flight in two bat species using time-resolved wake visualization, Journal of the Royal Society Interface 8 (2011) 1418–1428.
[12] U.M. Lindhe-Norberg, Y. Winter, Wing beat kinematics of a nectar feeding bat, Glossophaga soricina, flying at different flight speeds and Strouhal numbers, Journal of Experimental Biology 209 (2006) 3887–3897.
[13] F.T. Muijres, G.R. Spedding, Y. Winter, A. Hedenström, Actuator disk model and span efficiency of flapping flight in bats based on time-resolved PIV measurements, Experiments in Fluids 51 (2011) 511–525.
[14] E.V. Laitone, Wind tunnel tests of wings at Reynolds numbers below 7000, Experiments in Fluids 23 (1997) 405–409.
[15] M. Chadha, C.F. Moss, S.J. Sterbing-D'Angelo, Organization of the primary somatosensory cortex and wing representation in the Big Brown Bat, Eptesicus fuscus, Journal of Comparative Physiology 197 (2011) 89–96.
[16] S. Sterbing-D'Angelo, M. Chada, C. Chiu, B. Falk, W. Xian, J. Barcelo, J.M. Zook, C.F. Moss, Bat wing sensors support flight control, Proceedings of the National Academy of Sciences 108 (2011) 11291–11296.
[17] H. Soueid, L. Guglielmini, C. Airiau, A. Bottaro, Optimization of the motion of a flapping airfoil using sensitivity functions, Computers & Fluids 38 (2009) 861–874.
[18] Y. Sudhakar, S. Vengadesan, Flight force production by flapping insect wings in inclined stroke plane kinematics, Computers & Fluids 39 (2010) 683–695.
[19] M.H. Dickinson, F.-O. Lehmann, S.P. Sane, Wing rotation and the aerodynamic basis of insect flight, Science 284 (1999) 1954–1960.
[20] T.Y. Hubel, C. Tropea, Experimental investigation of a flapping wing model, Journal of Experimental Biology 46 (2008) 945–961.
[21] T.Y. Hubel, C. Tropea, The importance of leading edge vortices under simplified flapping flight conditions at the size scale of birds, Journal of Experimental Biology 213 (2010) 1930–1939.
[22] G. Bunget, BATMAV – A bio-inspired micro-aerial vehicle for flapping flight, 2010.

[23] M.A. Horner, T.H. Fleming, C.T. Sahley, Foraging behaviour and energetics of a nectar-feeding bat, Leptonycteris curasoae (Chiroptera: Phyllostomidae), Journal of Zoology 244 (1998) 575–586.

[24] C.T. Sahley, M.A. Horner, T.H. Fleming, Flight speeds and mechanical power outputs of the nectar-feeding bat, Leptonycteris curasoae (Phyllostomidae: Glossophaginae), Journal of Mammalogy 74 (1993) 594–600.

[25] S.M. Swartz, J. Iriarte-Diaz, D.K. Riskin, Wing structure and the aerodynamic basis of flight in bats, American Institute of Aeronautics and Astronautics Journal (2007) 2007–2042.

[26] S.M. Swartz, M.S. Groves, H.D. Kim, W.R. Walsh, Mechanical properties of bat wing membrane skin, Journal of Zoology 239 (1996) 357–378.

[27] S.M. Swartz, K.M. Middleton, Biomechanics of the bat limb skeleton: Scaling material properties and mechanics, Cells Tissues Organs 187 (2008) 59–84.

[28] C.J. Pennycuick, T. Alerstam, A. Hedenström, A new low-turbulence wind tunnel for bird flight experiments at Lund University, Sweden, Journal of Experimental Biology 200 (1997) 1441–1449.

[29] T.L. Hedrick, Software techniques for two- and three-dimensional kinematic measurements of biological and biomimetic systems, Bioinspiration & Biomimetics 3 (2008) 034001, 6 pp.

[30] R.J. Adrian, K.T. Christensen, Z.C. Lui, Analysis and interpretation of instantaneous turbulent velocity fields, Experiments in Fluids 29 (2000) 275–290.

[31] D. Lentink, Exploring the biofluiddynamics of swimming and flight, PhD Thesis, Wageningen University, 2008.

[32] D. Lentink, M.H. Dickinson, Rotational accelerations stabilize leading edge vortices on revolving fly wings, Journal of Experimental Biology 212 (2009) 2705–2719.

[33] E.R. Dumont, Bone density and the lightweight skeletons of birds, Proceedings of the Royal Society B 277 (2010) 2193–2198.